Poly(Amidoamine) Dendrimer Modified Superparamagnetic Nanoparticles as an Efficient Adsorbent for Cr(VI) Removal: Effect of High-Generation Dendrimer on Adsorption Performance

Can Cui[1] · Ya-Dian Xie[1] · Jiao-Jiao Niu[1] · Hai-Liang Hu[1] · Sen Lin[2]

Abstract

In this work, three different generations of Poly(amidoamine) dendrimers (PAMAM) decorated on magnetic Fe_3O_4 composites ($Fe_3O_4@SiO_2$–G1, $Fe_3O_4@SiO_2$–G3, $Fe_3O_4@SiO_2$–G5) were fabricated and characterized by FTIR, XRD, TEM, TGA, VSM and XPS. The obtained composites were used for Cr(VI) removal. Batch adsorption studies showed that the adsorption reached equilibrium within 60 min, and the optimal pH was 3.0. The result of adsorption kinetics was simulated by the pseudo-second-order model. The adsorption equilibrium isotherm was well fitted with the Langmuir adsorption model. Furthermore, thermodynamics calculations revealed that the adsorption process was endothermic and spontaneous. Importantly, adsorption capacity of Cr(VI) obeyed the sequence of $Fe_3O_4@SiO_2$–G1 $<$ $Fe_3O_4@SiO_2$–G5 $<$ $Fe_3O_4@SiO_2$–G3, 3 generation of PAMAM (G3) was the optimal for adsorption capacity of Cr(VI). The maximum theoretical Cr(VI) adsorption capacity (q_m) of $Fe_3O_4@SiO_2$–G3 was 334.45 mg/g, and removal ration remained above 89.5% after five cycles of adsorption–desorption. Thus, $Fe_3O_4@SiO_2$–G3 is predicted to be an efficient adsorbent for the adsorption of Cr(VI) from aqueous solution, and the obtained results can help in the generation optimization during fabrication of dendrimer modified adsorbents.

Keywords Superparamagnetic Fe_3O_4 · Poly(amidoamine) dendrimer · Generation · Adsorption · Cr(VI)

1 Introduction

Water contamination arises from heavy metal ions has attracted great attention due to its high toxicity, non-degradability, carcinogenicity, and ecological unbalance [1–3]. Of the heavy metals, chromium is widely used in the fields of electroplating, cement production, paper processing and textile industry [4]. Chromium ion is harmful to the environment and human health because of its biological build-up and tremendous toxicity. Cr(III) and Cr(VI) are the primary Cr ion states in aqueous solution. The latter is more toxic and carcinogenic [5]. Therefore, the development of low cost

materials and effective techniques for the removal of Cr(VI) is imperative.

A various number of water treatment processes like chemical precipitation [6], oxidation–reduction [7], ion exchange [8, 9], electrodialysis [10], membrane filtration, photocatalysis [11–13] and adsorption [14, 15] have been employed to decontaminate heavy metal pollution. Adsorption has been found out to serve as an efficient and economical technology for dealing with Cr(VI) due to its easy operation, low cost and environmentally friendly. To date, Numerous adsorbents including activated carbon [16], biological adsorbent [17], resin [18] and magnetic nanoparticles [19] have been extensively applied for Cr(VI) removal. Among these materials, magnetic nanoparticle Fe_3O_4 is the most attractive due to its advantages of biocompatibility, cheap price and especially superparamagnetic characteristics [20], that is widely applied in the fields of electrode, drug delivery, catalyst, thermal therapy, adsorption and so on [21–25]. Magnetic separation adsorbent based on Fe_3O_4 nanoparticle is outstanding due to its convenience and high efficiency. However, naked Fe_3O_4 nanoparticle is easy to be oxidized in air and aggregated in solution, that reduces

Can Cui and Ya-Dian Xie have contributed equally to this work.

✉ Sen Lin
linsen@mail.gyig.ac.cn

[1] School of Chemical Engineering, Guizhou Minzu University, Guiyang 550025, China

[2] Key Laboratory of High-Temperature and High-Pressure Study of the Earth's Interior, Institute of Geochemistry, Chinese Academy of Sciences, Guiyang 550081, China

its adsorption ability and selectivity for heavy metal ions. Surface-modified with functional groups is the most efficient method to overcome these disadvantages [26]. The surface of Fe_3O_4 nanoparticle is easy to be functionalized by silica [27], amine groups [28], oxygen-containing groups (carboxyl, hydroxyl) [29–31] and sulfur-containing groups (sulfhydryl, sulfonic acid) [32]. The existence of these substances can improve the stability of Fe_3O_4 nanoparticles and prevent aggregation. Sharma et al. [27] designed a visible light active photocatalyst $Fe_3O_4/ZnO/Si_3N_4$ for the degradation of dyes from aqueous solution, that Si_3N_4– as an effective support for metal oxides to avoid the agglomeration. In addition, functional groups can selectively adsorb specific heavy metal ions through complexation effect, electrostatic attraction or ion exchange, thus improving the adsorption selectivity and capacity. For instance, Alhokbany et al. prepared Schiff base polymer decorated magnetic Fe_3O_4 composite (MPOP) for removing of Cd(II) and Hg(II) from aqueous solution, the interaction between N atom and metal ion dominated the adsorption of Cd(II) and Hg(II) [33]. Fu et al. fabricated magnetic Fe_3O_4-encapsulated C3N3S3 polymer/reduced graphene oxide composite [rGO-poly(C3N3S3)/Fe_3O_4] for aqueous Pb(II) and Hg(II) removal, adsorption mechanism is that Hg(II) preferentially binds to sulfur functional groups and Pb(II) tends to be adsorbed by nitrogen groups in poly(C3N3S3) matrix [34].

Poly(amidoamine) dendrimer (PAMAM) is regarded as a kind of biopolymer, which is widely studied in many fields, such as drug delivery, gene therapy, ultrasensitive sensor, catalyst carrier and adsorption in wastewater treatment, because of its excellent biocompatibility, highly branched three-dimensional structure, lots of reactive terminal groups, and monodispersed molecular weight [35–37]. Tremendous amine groups located within its interior and its surface enable PAMAM to bind with heavy metal ions by complexation effect, ion exchange and electrostatic attraction [38]. Nevertheless, PAMAM dendrimer is easily soluble in aqueous media, which makes its separation/recovery difficult to recycle. So PAMAM dendrimer is usually anchored on support substances such as silica [39, 40], graphene [41], and magnetic substance [42]. Furthermore, adsorption capacity is related to the dendrimer generation of PAMAM. Niu et al. found that the increase of adsorption capacity of Hg(II) and Ag(I) with dendrimer generation (G2 > G1 > G0.5), which is attributed to high content of sulfur group that high generation dendrimer possess [43]. However, as we all known that with the increase of generation, the steric hindrance increases, and serious surface defects of PAMAM appears, thus the adsorption capacity must be affected. As far as we know, the influence of high-generation dendrimer of PAMAM on adsorption capacity for Cr(VI) has not been studied.

In this work, three different generations of PAMAM dendrimer were immobilized on magnetic Fe_3O_4 composites ($Fe_3O_4@SiO_2$–G1, $Fe_3O_4@SiO_2$–G3, $Fe_3O_4@SiO_2$–G5) to combine the merits of the two components for the efficient removal of Cr(VI), and compared the adsorption capacity of Cr(VI) between the three different adsorbents. The effective factors on the adsorption capability such as adsorbent dosage, adsorption time, temperature, initial concentration and pH of sample solution were examined and optimized. In addition, the adsorption isotherms, adsorption kinetics, thermodynamic and reusability were investigated to evaluate the adsorption properties and adsorption mechanism.

2 Materials and Methods

2.1 Materials

Ferric chloride ($FeCl_3$), ferrous chloride tetrahydrate ($FeCl_2 \cdot 4H_2O$), sodium hydroxide, 1,2–diaminoethane and methyl acrylate were purchased from Sinopharm Chemical Reagent Co. Ltd., China. 3–aminopropyltrimethoxysilane (APTMS) was obtained from Shanghai Aladdin Bio–Chem Technology Co. Ltd., China. Potassium dichromate ($K_2Cr_2O_7$) was obtained from Sigma–Aldrich (St. Louis, MO, USA). All the chemicals were of analytical grade. 1,2–diaminoethane and methyl acrylate were distilled before use, and other reagents were used as received without further purification. Deionized water was used throughout the experiment.

2.2 Characterization

The synthetic materials were characterized by Fourier–transform infrared spectra (FTIR), X–ray powder diffraction (XRD), transmission electron microscopy (TEM), Thermogravimetric analysis (TGA), Vibrating sample magnetometer (VSM) and X–ray photoelectron spectroscopy (XPS). FTIR spectra were obtained on a Perkin–Elmer Spectrometer in the range from 4000 to 400 cm^{-1}. The crystalline structure of Fe_3O_4, $Fe_3O_4@SiO_2$–G1, $Fe_3O_4@SiO_2$–G3 and $Fe_3O_4@SiO_2$–G5 were characterized by XRD (PANalytical Empyrean, Netherlands) with Cu Ka radiation (k = 1.54178 Å) at a scanning rate of 2°/min in the 2θ range from 4° to 70°. The particle size and morphology of nanocomposites were observed by TEM (JEM–2010 (HT)). TGA measurements were performed on Diamond TG/DTA 6300 (Perkin–Elmer USA) at a heating rate of 5 °C/min under nitrogen. Magnetic hysteresis loops were characterized by VSM (Lakeshore 7404) at room temperature with a maximum external field of Hm = 200,000 Oe. The surface element composition and element valence of the adsorbent were characterized by XPS

Scheme 1 The synthetic procedures for adsorbents
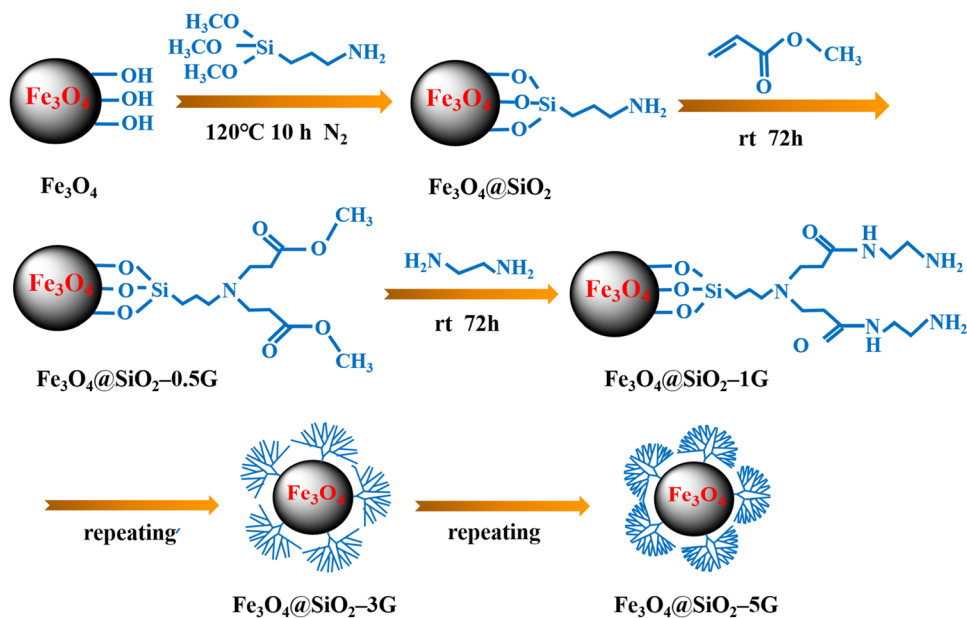
(Thermo Scientific K-Alpha) with Al Kα ray source and C 1s (284.80 eV) for calibration.

2.3 Preparation Procedure

The synthetic route of $Fe_3O_4@SiO_2$–G1, $Fe_3O_4@SiO_2$–G3 and $Fe_3O_4@SiO_2$–G5 is presented in Scheme 1. Briefly, APTMS coated Fe_3O_4 was synthesized according to the reported method [44, 45]. About 3.0 g of APTMS coated Fe_3O_4 and 5.0 mL of methyl acrylate were dispersed in 80 mL methanol under N_2. The suspension was reacted at room temperature for 72 h. The resulting particles were washed with methanol and then reacted with 10.0 mL 1,2–diaminoethane in 100 mL methanol at room temperature for another 72 h. After that, $Fe_3O_4@SiO_2$–G1 was obtained after separation and the subsequent washed with ethanol. The above reaction cycles (Michael addition and amidation reaction) were repeated until 3 generation of PAMAM dendrimer modified Fe_3O_4 ($Fe_3O_4@SiO_2$–G3) and 5 generation of PAMAM dendrimer modified Fe_3O_4 ($Fe_3O_4@SiO_2$–G5) were obtained. It was noteworthy that the addition amount of methyl acrylate and 1,2–diaminoethane increased with the increase of the dendrimer generation, which was kept at 50% excess and 2 times, respectively. The obtained composites were washed with methanol and dried in vacuum at 50 °C for 12 h.

2.4 Batch Adsorption Experiments

$K_2Cr_2O_7$ was dissolved with deionized water as a stock Cr(VI) solution (1000 mg/L). The Cr(VI) solutions with different initial concentrations were prepared by dilution of the stock Cr(VI) standard solution with deionized water. The effects of five parameters on the adsorption of Cr(VI) by $Fe_3O_4@SiO_2$–G1, $Fe_3O_4@SiO_2$–G3 and $Fe_3O_4@SiO_2$–G5 were studied. The range of the tested parameters was as follows: initial pH (3–10), adsorbent dosage (4–16 mg), adsorption time (10–150 min), temperature (293–308 K), and initial Cr(VI) concentration (10–120 mg/L). For a typical example, when measuring the effect of the adsorption time, 10 mg of adsorbent was added into a 150 ml stoppered conical flask containing 50 ml of 50 mg/L Cr(VI) solution, with an initial pH of 3.0, and shaking with 150 rpm at 303 K. After designated time periods (10, 15, 20, 30, 40, 60, 90, 120, 150 min), the Cr(VI) solution samples were collected by a 5 mL syringe and filtered immediately through a 0.45 μm microfiltration membrane. The concentration of Cr(VI) was determined by atomic absorption spectrophotometry (AAS, AA240FS–GTA120, USA) [46]. The pH was regulated by HCl (0.1 M) and NaOH (0.1 M). All experiments were carried out triplicate in order to effectively reduce the experimental error.

The difference between the initial concentration and the adsorption equilibrium concentration is allowed to evaluate the amount of metal ion adsorbed. The equilibrium adsorption capacity (q_e, mg/g) of the absorbent towards Cr(VI) is calculated by Eq. (1) [43]:

$$q_e = \frac{(C_0 - C_e) \times V}{m},\tag{1}$$

where C_0 and C_e (mg/L) are the initial and equilibrium concentrations of Cr(VI) in the solution, respectively, V (L) is the volume of the solution, and m (g) represents the weight of adsorbent.

3 Results and Discussion

3.1 Characterization of the Adsorbents

FTIR spectra of Fe_3O_4, $Fe_3O_4@SiO_2$–G1, $Fe_3O_4@SiO_2$–G3 and $Fe_3O_4@SiO_2$–G5 are presented in Fig. 1a. Both in the FTIR spectra of Fe_3O_4 and PAMAM dendrimer functionalized Fe_3O_4 composites, we all observed the absorption peak at 598 cm^{-1} due to the vibration of Fe–O. Compared with unmodified Fe_3O_4, $Fe_3O_4@SiO_2$–G1, $Fe_3O_4@SiO_2$–G3 and $Fe_3O_4@SiO_2$–G5 possessed absorption bands at 2925 cm^{-1} and 2853 cm^{-1} due to the vibration of the CH_2 group, absorption bands at 1632 cm^{-1}, 1518 cm^{-1} and 1429 cm^{-1} due to the vibration of –CO–NH– group, and at 1147 cm^{-1} belongs to Si–O–Si [47], which indicates the successful decoration of Fe_3O_4 with PAMAM.

The XRD patterns of Fe_3O_4, $Fe_3O_4@SiO_2$–G1, $Fe_3O_4@SiO_2$–G3 and $Fe_3O_4@SiO_2$–G5 are shown in Fig. 1b. The XRD of Fe_3O_4 shows the typical (220), (311), (400), (422), (511), and (440) crystal planes at 30.12°, 35.43°, 43.09°, 53.49°, 57.18°, and 62.63°, respectively [32]. After decoration of Fe_3O_4 with different generations of PAMAM dendrimer, the characteristic peaks of the above crystal planes still exist and do not change the position and intensity,

suggesting the crystal structure of Fe_3O_4 is not destroyed during the functionalization.

The grafted dendrimer content of $Fe_3O_4@SiO_2$–G1, $Fe_3O_4@SiO_2$–G3 and $Fe_3O_4@SiO_2$–G5 can be calculated from TGA. As shown in Fig. 1c, the first stage weight loss for water evaporation is observed in the range of 50–115 °C, about 1.99%, 2.55% and 1.96% water loss for $Fe_3O_4@SiO_2$–G1, $Fe_3O_4@SiO_2$–G3 and $Fe_3O_4@SiO_2$–G5, respectively. Then, the slight weight loss from 115 to 230 °C can be observed due to the decomposition of silica. After that, a sharp decrease of the weight loss between 230 and 700 °C due to the decomposition of PAMAM dendrimer. The final mass losses are 4.9%, 12.1% and 24.3% for $Fe_3O_4@SiO_2$–G1, $Fe_3O_4@SiO_2$–G3 and $Fe_3O_4@SiO_2$–G5, respectively, which imply that the modified organic matter percentage increases with generation of PAMAM dendrimer increases.

Particle size and morphology of Fe_3O_4, $Fe_3O_4@SiO_2$–G3 before and after adsorption of Cr(VI) were determined by TEM. As shown in Fig. 2a, Fe_3O_4 are dispersed as homogeneously distributed individual NPs with well–defined spherical shapes that are around 6–8 nm in diameter. Figure 2b shows the morphology of $Fe_3O_4@SiO_2$–G3 before adsorption. Because PAMAM dendrimer do not significantly attenuate electron beams under TEM, $Fe_3O_4@SiO_2$–G3 are largely present as isolated clusters with a spherical shape, approximately 30 nm, further indicating the successful

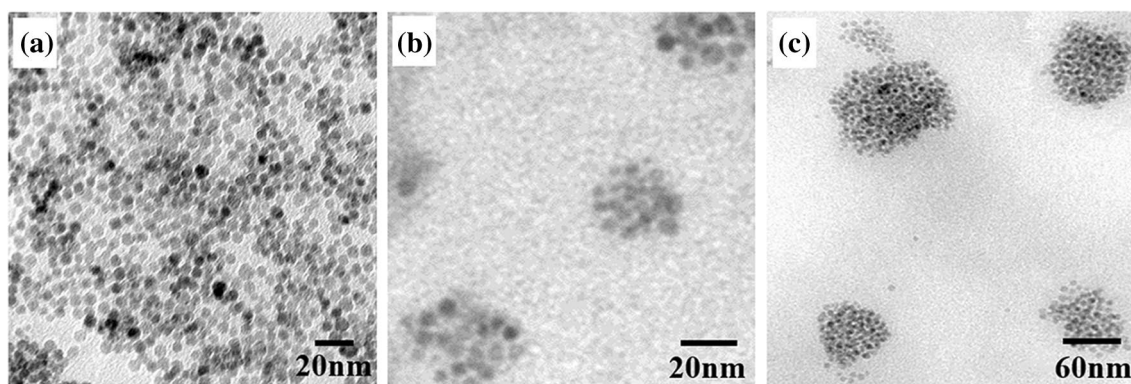**Fig. 1** The FTIR (**a**), XRD (**b**) and TGA (**c**) characterization
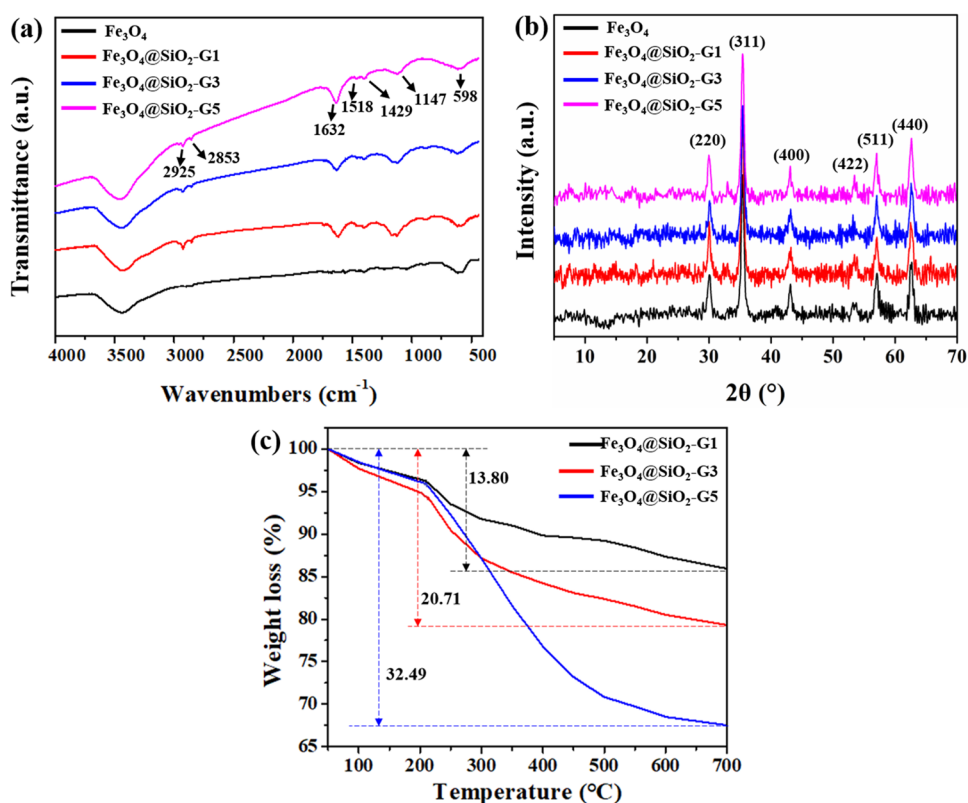
Fig. 2 TEM micrographs of Fe$_3$O$_4$ nanoparticles (**a**) and Fe$_3$O$_4$@SiO$_2$–G3 before (**b**) and after (**c**) adsorption
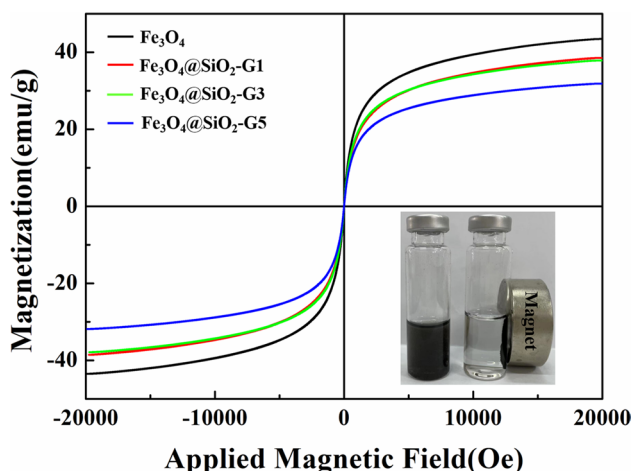
Fig. 3 Magnetic property of Fe$_3$O$_4$ and the nanocomposites

Fig. 4 Effect of pH on adsorption capacity. (C_0 = 50 mg/L; adsorbent dosage = 10 mg; t = 60 min; T = 303 K)

encapsulation of Fe$_3$O$_4$ by PAMAM dendrimer. Comparing the change of Fe$_3$O$_4$@SiO$_2$–G3 after adsorption, it can be seen that Fe$_3$O$_4$@SiO$_2$–G3 is also existed as isolated cluster with a nearly spherical shape, but the cluster size increases, with the size of about 70 nm (Fig. 2c). This phenomenon may be due to the electrostatic attraction between Cr(VI) and the adsorbent.

The magnetic hysteresis loops of Fe$_3$O$_4$ and the nanocomposites are shown in Fig. 3, the coercivity and magnetic remanence are almost zero for them, indicating superparamagnetic nature of the adsorbents. The saturation magnetization is 38.55, 37.88 and 31.86 emu/g for Fe$_3$O$_4$@SiO$_2$–G1, Fe$_3$O$_4$@SiO$_2$–G3, and Fe$_3$O$_4$@SiO$_2$–G5, which decreases by 4.90, 5.57, and 11.59 emu/g respectively as compared with Fe$_3$O$_4$, indicating that amounts of nonmagnetic matter is covered on the surface of Fe$_3$O$_4$ magnetic core, which further proving the successful preparation of nanocomposites. The remaining saturation magnetization in nanocomposites is still adequate for their efficient separation by using an external magnetic field [45]. As shown in Fig. 3(inset), the
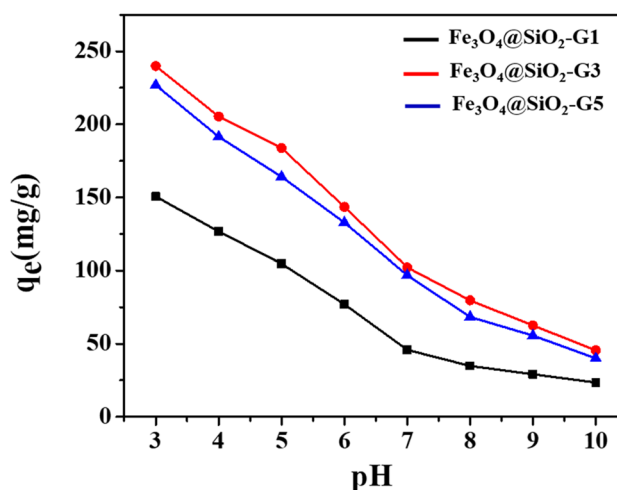
black homogeneous dispersion of Fe$_3$O$_4$@SiO$_2$–G3 is easily attracted to the wall of vial in the presence of an external magnetic field. The results demonstrate that as-synthetic nanocomposites can be rapidly separated and recovered from solution by simple magnetic separation owing to the strong superparamagnetism, thus facilitating manipulation in the practical applications.

3.2 Effect of Solution pH for Cr(VI) Removal

The solution pH has considerable effect on metal ion adsorption as it influences not only on the existing forms of heavy metal ion, but also the surface charge of an adsorbent. To investigate the optimal pH value for Cr(VI) removal, a series of experiments with different initial pH (3–10) were carried out. As presented in Fig. 4, With the solution pH increases from 3 to 10, the adsorption for Cr(VI) is gradually decreased for the three adsorbents. This is attributed to the different forms of chromium

in the aqueous solution at different pH values. When pH > 6, CrO_4^{2-} is the primary form, while $Cr_2O_7^{2-}$ and $HCrO_4^-$ are predominant at pH 2–6 [48]. The maximum Cr(VI) adsorption capacity is obtained at pH 3, which is partly attributed to the strong electrostatic interactions between anions ($Cr_2O_7^{2-}$ and $HCrO_4^-$) and protonated imidazole N^+ in the three adsorbents. When the solution pH is greater than 3, due to the deprotonation of N and an increase in the number of bivalent anions (CrO_4^{2-}), both enhance the electrostatic repulsion of the adsorbents and chromium ions, which decline the adsorption capacity for Cr(VI).

Furthermore, the adsorption capacity decreases by the sequence of $Fe_3O_4@SiO_2$–G3 > $Fe_3O_4@SiO_2$–G5 > $Fe_3O_4@SiO_2$–G1, the adsorption capacity of $Fe_3O_4@SiO_2$–G3 and $Fe_3O_4@SiO_2$–G5 are stronger than that of $Fe_3O_4@SiO_2$–G1, which is attributed to lower content of amine groups that $Fe_3O_4@SiO_2$–G1 possess. But interestingly we found that the adsorption capacity of $Fe_3O_4@SiO_2$–G5 was relatively poor than that of $Fe_3O_4@SiO_2$–G3. This may be due to excessively high generation not only causes the large sterically hindrance, which hinders the contact of chromium ions with the amine groups located within the interior of PAMAM, but also causes serious surface defects of PAMAM, that decreasing amine groups on the surface of $Fe_3O_4@SiO_2$–G5. The above result indicates that the affinity of the composites increases with dendrimer generation increases only in low generation range, but excessively high generation of PAMAM is unfavourable for the adsorption. Above all, the optimal pH is 3.0, which is selected for the subsequent experiments. In addition, the removal of Cr(VI) is affected by generation of PAMAM dendrimer, 3 generation of PAMAM (G3) is the optimal for adsorption capacity of Cr(VI).

3.3 Effect of Adsorbent Dosage for Cr(VI) Removal

Adsorbent dose is an important factor which determines the presence of number of active sites on the surface of adsorbent [49]. The adsorption capacity of Cr(VI) varies with the adsorbent dosage. Figure 5 shows the effect of the mass of adsorbent on the adsorption of Cr(VI). It is observed that the adsorption capacity decreases with the increase in the adsorbent dose, the adsorption capacity of Cr(VI) by $Fe_3O_4@SiO_2$–G3 decreases from 438.75 to 155.16 mg/g with the dosage increases from 4 to 16 mg, this effect can be explained by the active sites of adsorbent are not be completely occupied by chromium ions at high dosages of adsorbent. To consider operation consumption, while also ensuring a high adsorption capacity, the requirement of active sites was fulfilled at 10 mg dose for concentration of 50 mg/L, and q_e was 239.75 mg/g.
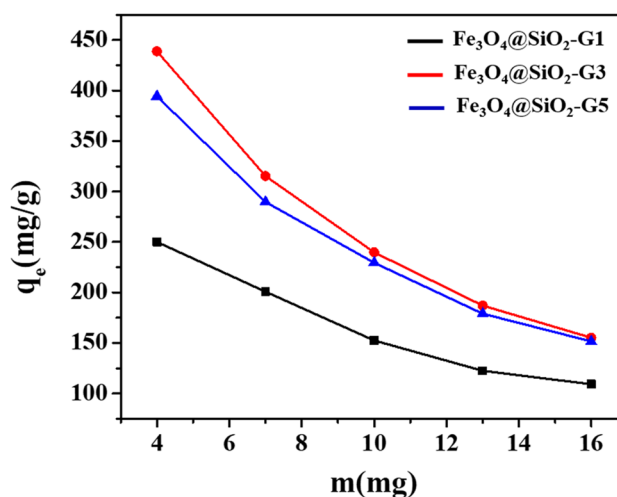

Fig. 5 Effect of adsorbent dosage on adsorption capacity. ($C_0 = 50$ mg/L; pH 3.0; $t = 60$ min; $T = 303$ K)

3.4 Effect of Temperature for Cr(VI) Removal and Thermodynamic Study

The effect of temperature of Cr(VI) adsorption on adsorbent was investigated in the temperature range 293–308 K. As shown in Fig. 6a, it is noticed that an increase in temperature promotes an increase in the amount of Cr(VI) adsorbed by all adsorbents, which indicates that the adsorption process of Cr(VI) is endothermic. This is attributed to the increment in the kinetic energy of the adsorbent molecules with the increment in temperature, the increased activated sites created on the adsorbents, and the increase in kinetic motion of chromium ions.

The different thermodynamic parameters of adsorption can reflect its spontaneity, randomness, endothermicity or exothermicity. Thermodynamic parameters such as standard free enthalpy ΔG^0 is calculated with Eq. (3), standard enthalpy ΔH^0 and standard entropy ΔS^0 are calculated from the slope and intercept of the plot of K_d versus $1/T$ (Fig. 6b) using Eq. (4) [50]:

$$K_d = \frac{aq_e}{C_e} \tag{2}$$

$$\Delta G^0 = -RT \ln K_d = \Delta H^0 - T\Delta S^0 \tag{3}$$

$$\ln K_d = \left(\frac{\Delta S^0}{R}\right) - \left(\frac{\Delta H^0}{R}\right)\frac{1}{T}, \tag{4}$$

where K_d is the distribution constant; a (g/L) is the adsorbent dose; q_e (mg/g) is the adsorption capacity at equilibrium; C_e (mg/L) is the concentration at equilibrium of adsorbate in solution; ΔG^0 (kJ/mol) is the standard Gibbs energy change;
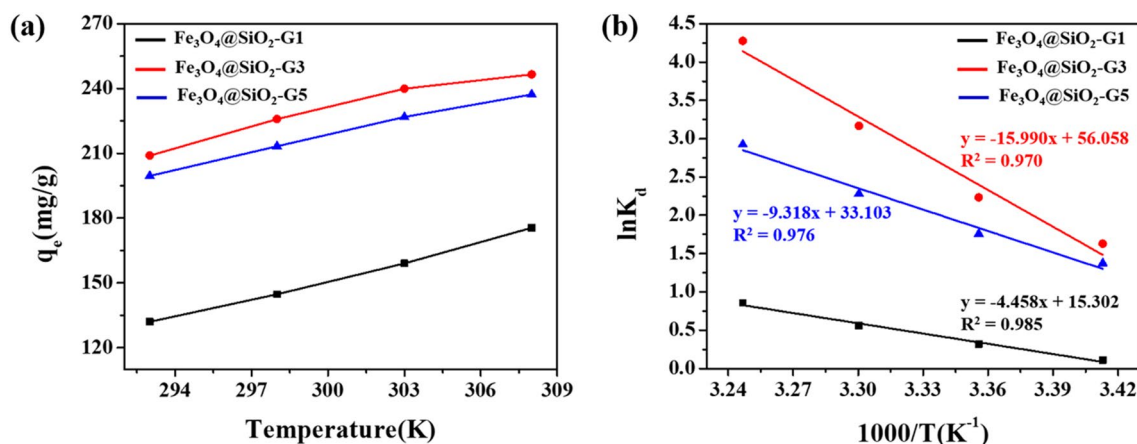
Fig. 6 Effect of temperature on the adsorption capacity (**a**) and evolution of $\ln K_d$ as function of $1000/T$ (**b**). ($C_0 = 50$ mg/L; pH 3.0; adsorbent dosage = 10 mg; $t = 60$ min)

R (8.314 J/mol/K) is the ideal gas constant; T (K) is the absolute temperature; ΔH^0 (kJ/mol) is the standard enthalpy change, and ΔS^0 (J/mol/K) is the standard entropy change. The thermodynamic parameters of the adsorption at different temperatures are summarized in Table 1. ΔG^0 values are negative for adsorption of Cr(VI) onto the adsorbents. This demonstrates that the adsorption procedure is spontaneous and thermodynamically practicable. Furthermore, the ΔG^0 value decreases as the temperature increases, demonstrating adsorption is more favorable at high temperature. Meanwhile the positive values of ΔS^0 indicate increased disorder at the adsorbate–adsorbent interface during adsorption of Cr(VI) on the adsorbent surface. Additionally, the values of ΔH^0 are positive, which suggests that the adsorption process on the surface is an endothermic process [50], and the ΔH^0 values of $Fe_3O_4@SiO_2$–G1, $Fe_3O_4@SiO_2$–G3 and $Fe_3O_4@SiO_2$–G5 is 37.06, 132.94 and 77.47 kJ/mol, respectively, indicating that interaction force between adsorbents and chromium ions increases by the sequence of $Fe_3O_4@SiO_2$–G1 $<$ $Fe_3O_4@SiO_2$–G5 $<$ $Fe_3O_4@SiO_2$–G3, which is consistent with the adsorption capacity results.

3.5 Kinetic Studies on Cr(VI) Removal

To investigate the adsorption rate of Cr(VI) on adsorbents and measure the adsorption equilibrium, the adsorption

kinetics were studied. The adsorption kinetic plots of the adsorbents for Cr(VI) are illustrated in Fig. 7a. The adsorption of the adsorbent proceeds speedily during 0–40 min. Then, it conducts relaxedly and approaches equilibrium at 60 min. The equilibrium adsorption capacity of $Fe_3O_4@SiO_2$–G1, $Fe_3O_4@SiO_2$–G3 and $Fe_3O_4@SiO_2$–G5 for Cr(VI) is 150.80, 240.55 and 227.55 mg/g, respectively. The sharp increase in the initial stage is mainly due to the presence of abundant active sites on adsorbents and high concentration of Cr(VI), which facilitates the contact of active adsorption sites with chromium ions, leading to the rapid capture of chromium ions by the adsorbents [48]. When the adsorption time continues to extend, Cr(VI) concentration reduces, and the active adsorption sites of the adsorbent are largely occupied by chromium ions, decreasing the contact opportunity and resulting in the decrease of adsorption rate until approach equilibrium. To ensure the system reached adsorption equilibrium, the contact time was set to 60 min in the following experiments.

To explore the adsorption mechanism, the experimental data were fitted by kinetic equations, and the correlation coefficients were obtained. The two equations represent the pseudo-first-order kinetic model and pseudo-second-order kinetic model, which can be described below in Eqs. (5) and (6) [51]:

Pseudo-first-order equation:

Table 1 Thermodynamic parameters for the adsorption of Cr(VI) on adsorbents at different temperatures

Adsorbent	Gibbs free energy ΔG^0 (kJ/mol)				Enthalpy ΔH^0 (kJ/mol)	Entropy ΔS^0 (J/mol/K)
	293 K	298 K	303 K	308 K		
$Fe_3O_4@SiO_2$–G1	−0.215	−0.852	−1.488	−2.124	37.06	127.22
$Fe_3O_4@SiO_2$–G3	−3.619	−5.949	−8.279	−10.610	132.94	466.07
$Fe_3O_4@SiO_2$–G5	−3.169	−4.546	−5.922	−7.298	77.47	275.22

Fig. 7 Adsorption kinetics (**a**), pseudo-first-order fitting plots (**b**) and pseudo-second-order fitting plots (**c**) for Cr(VI). ($C_0 = 50$ mg/L; pH 3.0; adsorbent dosage = 10 mg; $T = 303$ K)
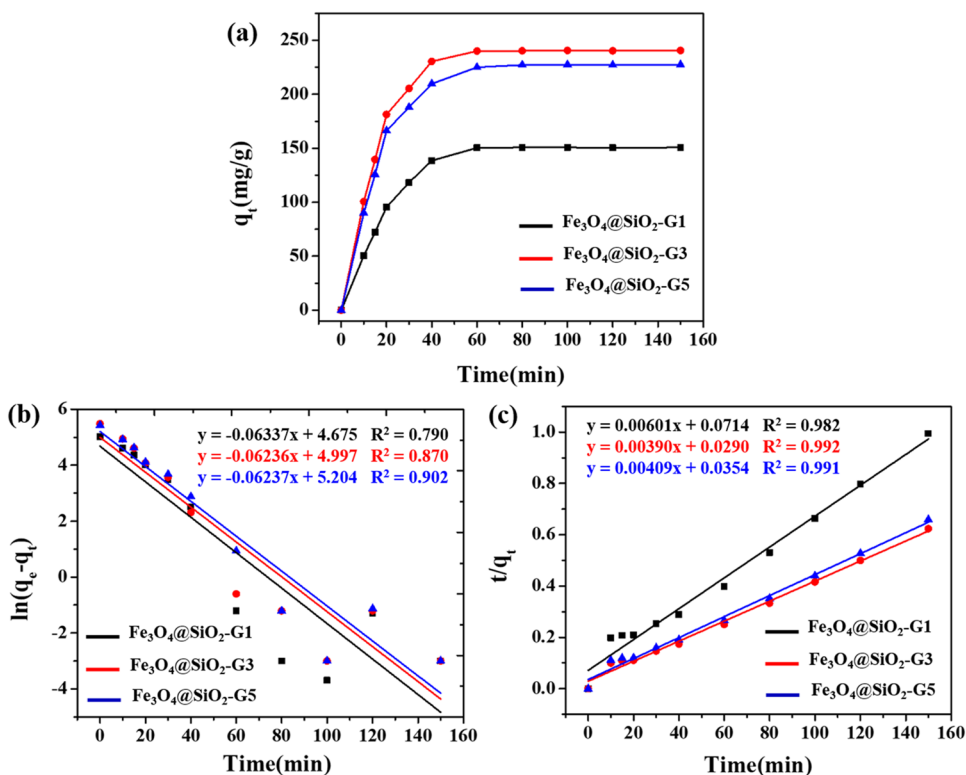
$$\ln(q_e - q_t) = \ln q_e - k_1 t \tag{5}$$

Pseudo-second-order equation:

$$\frac{t}{q_t} = \frac{1}{k_2 q_e^2} + \frac{t}{q_e}, \tag{6}$$

where q_e (mg/g) is the equilibrium adsorption amount of Cr(VI), q_t (mg/g) is the adsorption amount of Cr(VI) at time t (min), k_1 and k_2 are the equilibrium rate constant of pseudo-first-order adsorption and pseudo-second-order adsorption models, respectively.

The fitting curves and related parameters of the pseudo-first-order model and pseudo-second-order model are shown in Fig. 7b, c and Table 2. The adsorption kinetic for the three adsorbents fit Pseudo-second-order model well as indicated by the higher correlation coefficients (R^2). The calculated equilibrium adsorption capacity ($q_{e,cal}$) that derived from pseudo-second-order model is more in agreement with the experimental value ($q_{e,exp}$), further confirms the reasonable

of describing the adsorption kinetic process of Cr(VI) by pseudo-second-order model, suggesting that the chemical interactions are possibly involved in the adsorption processes. In the current work, an occurrence of chemical adsorption for the adsorbent can be understood as the complexation effect of chromium ions with the N- and O-containing groups on adsorbents. Furthermore, the generation of PAMAM with no impact on the adsorption mechanism.

3.6 Effect of Initial Concentration for Cr(VI) Removal and Adsorption Isotherms

The effect of the initial Cr(VI) concentration on the adsorption capacity of adsorbents for Cr(VI) was investigated. As shown in Fig. 8, with the increase of initial Cr(VI) concentration, the adsorption capacity of the three adsorbents gradually increase. The adsorption capacity of $Fe_3O_4@SiO_2$–G1, $Fe_3O_4@SiO_2$–G3 and $Fe_3O_4@SiO_2$–G5 is elevated from 39.4, 49.9 and 47.4 mg/g to 213.1, 331.8 and 312.6 mg/g respectively when the initial concentration

Table 2 Kinetics parameters for Cr(VI)

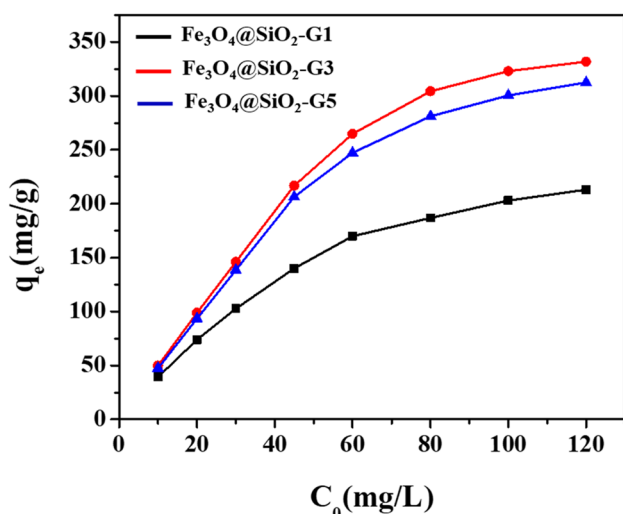| Adsorbent	$q_{e,exp}$ (mg/g)	Pseudo-first-order			Pseudo-second-order		
		$q_{e,cal}$ (mg/g)	k_1 (1/min)	R^2	$q_{e,cal}$ (mg/g)	k_2 (g/mg/min)	R^2
$Fe_3O_4@SiO_2$–G1	150.80	107.23	0.06337	0.790	166.39	0.00051	0.982
$Fe_3O_4@SiO_2$–G3	240.55	147.97	0.06236	0.870	256.41	0.00052	0.992
$Fe_3O_4@SiO_2$–G5	227.55	182.00	0.06237	0.902	244.50	0.00047	0.991

Fig. 8 Effect of Cr(VI) initial concentration on adsorption capacity. (pH 3.0; adsorbent dosage = 10 mg; T = 303 K; t = 60 min)

of Cr(VI) increases from 10 to 120 mg/L. The enhanced adsorption for Cr(VI) by the raising initial concentration is due to the high concentration gradient under high concentration, which promotes the diffusion of chromium ions to the active sites of the adsorbent. Therefore, the removal for Cr(VI) by the adsorbent is increased.

Two adsorption isotherms (i.e., Langmuir and Freundlich model) were used to describe the equilibrium adsorption according to Eqs. (7) and (8) [52]:

Langmuir adsorption isotherm:

$$\frac{C_e}{q_e} = \frac{1}{k_L q_m} + \frac{C_e}{q_m} \tag{7}$$

Freundlich adsorption isotherm:

$$\ln q_e = \ln k_F + \frac{1}{n} \ln C_e \tag{8}$$

where q_e (mg/g) and C_e (mg/L) are the amounts of Cr(VI) absorbed on adsorbent and the Cr(VI) concentration at adsorption equilibrium, respectively. k_L (L/mg) is the Langmuir constant related to the energy of adsorption, q_m (mg/g) refers to the maximum adsorption capacity, k_F and n are constants for the Freundlich isotherm. The fitting curves and relative parameters of each model are shown in Fig. 9 and Table 3. Compared with Freundlich model, Langmuir model provides better correlation coefficients ($R_L^2 > R_F^2$). This result demonstrates that the adsorption of Cr(VI) onto the nanocomposites sites follows a monolayer/homogenous pattern [53]. It is suggested that chromium ions are highly likely to interact with the active sites of the nanocomposites through a complexation process [43]. The maximum adsorption capacity (q_m) calculated by the Langmuir model is 245.10, 334.45, and 326.80 mg/g for Fe_3O_4@SiO_2–G1,
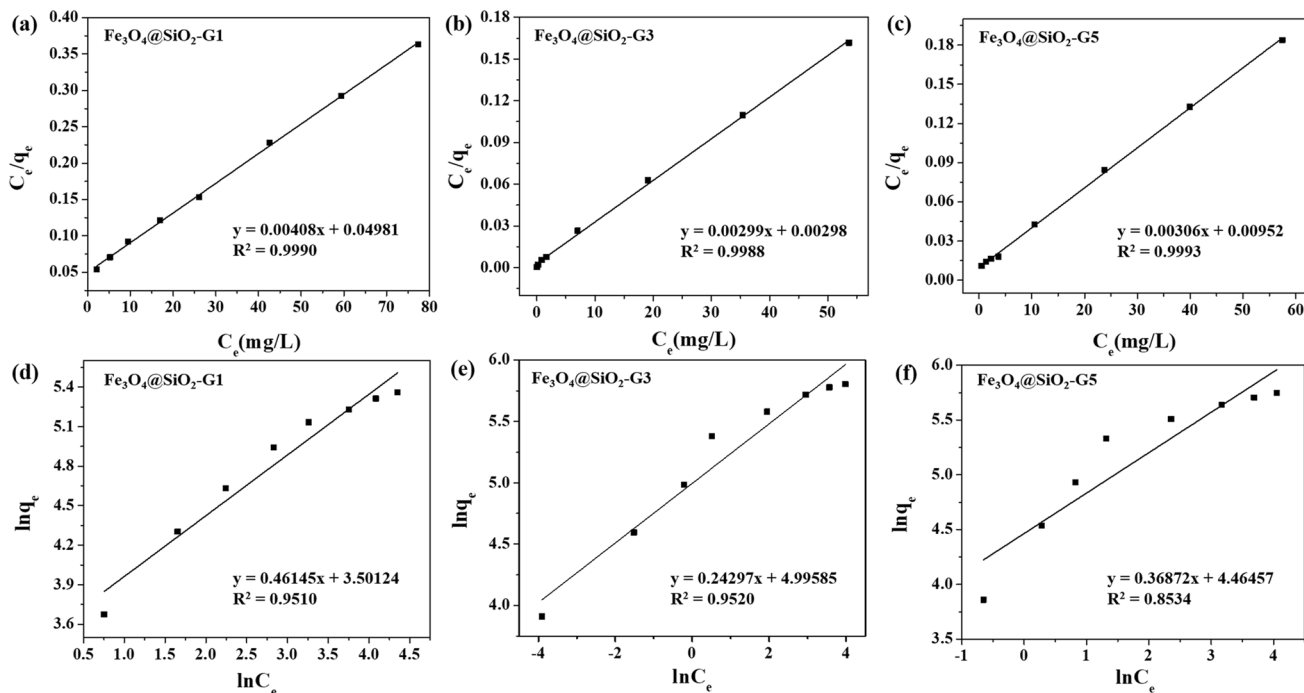

Fig. 9 Linearized form plot of Langmuir adsorption isotherm (**a–c**) and Freundlich adsorption isotherm (**d–f**) for the adsorption of Cr(VI)

Table 3 Isotherm parameters for Cr(VI)

Adsorbent	Langmuir model			Freundlich model		
	q_m (mg/g)	k_L (L/mg)	R_L^2	k_F (mg/g)	$1/n$	R_F^2
$Fe_3O_4@SiO_2$–G1	245.10	0.0819	0.9990	33.16	0.461	0.9510
$Fe_3O_4@SiO_2$–G3	334.45	1.0034	0.9988	147.80	0.243	0.9520
$Fe_3O_4@SiO_2$–G5	326.80	0.3214	0.9993	86.88	0.369	0.8534

Table 4 Comparison of q_m for Cr(VI) between the adsorbents

Adsorbents	q_m (mg/g)	References
$Fe_3O_4@SiO_2$–G3	334.45	This work
Chitosan/$NiFe_2O_4$ (CNF)	31.52	[19]
GO-DIL	260.92	[48]
ZFA-350	52.63	[50]
Fe_3O_4–FeB	38.9	[54]
Q-APEI	334.00	[55]
MBC/PPE	227.9	[56]
Co–Al–LDH@Fe_2O_3/3DPCNF	400.40	[57]
PPy/HMSNs	322	[58]
FSBC (1:1:1)	103.93	[59]

$Fe_3O_4@SiO_2$–G3 and $Fe_3O_4@SiO_2$–G5, respectively, indicating the adsorption capacity of $Fe_3O_4@SiO_2$–G3 is better than that of $Fe_3O_4@SiO_2$–G1 and $Fe_3O_4@SiO_2$–G5, which is consistent with the obtained results above. The adsorption equilibrium constant k_L increases by the sequence of $Fe_3O_4@SiO_2$–G1 < $Fe_3O_4@SiO_2$–G5 < $Fe_3O_4@SiO_2$–G3, which means that the binding strength of adsorbents and chromium ions increases by the same sequence. In addition, the $1/n$ values are all less than 1 computed by Freundlich model, revealing that the adsorption process proceed easily. The comparison of q_m between previous reported adsorbents and $Fe_3O_4@SiO_2$–G3 are presented in Table 4. The results show that $Fe_3O_4@SiO_2$–G3 has an excellent adsorption capacity for Cr(VI) and is an effective adsorbent.

3.7 XPS Study on Adsorption of Cr(VI) on $Fe_3O_4@SiO_2$–G3

To further investigate the adsorption mechanism, The XPS analysis of $Fe_3O_4@SiO_2$–G3 before and after adsorption was carried out. The XPS spectra is shown in Fig. 10, the peaks of Fe, O, N, C, Si are appeared in the XPS spectrum before adsorption in Fig. 10a. The O 1s high resolution spectrum of $Fe_3O_4@SiO_2$–G3 profile consists of three fitting peaks, including Si–O–Si, CONH and Fe–O centers at the binding energy of 533.42, 531.76, and 530.03 eV, respectively (Fig. 10c). As well as the N 1s consists of two fitting peaks of CONH and C–N groups, which centers at 400.39 and 398.68 eV, respectively (Fig. 10e).

After adsorption of Cr(VI), the peak of Cr 2p is presented in the XPS spectra (Fig. 10a), indicating the successful uptake of Cr(VI) onto $Fe_3O_4@SiO_2$–G3. From the high-resolution XPS spectrum (Fig. 10b), the optimum fitting is achieved by deconvoluting Cr 2p spectrum into four peaks. The peaks at 576.38 eV and 586.23 eV are ascribed to Cr (III) $2p_{3/2}$ and $2p_{1/2}$, respectively, while the peaks at 581.25 eV and 590.09 eV are belonged to Cr(VI) $2p_{3/2}$ and $2p_{1/2}$, respectively. The results indicated that the chromium adsorbed onto the surface of $Fe_3O_4@SiO_2$–G3 contained both Cr(III) and Cr(VI), because Cr(VI) was reduced to Cr(III) during adsorption.

The O1s peak of CONH changes from 531.76 to 531.90 eV after capture of Cr(VI) in Fig. 10d, but the O1s peaks of Si–O–Si and Fe–O have no change before and after adsorption. The N 1s peak of CONH group moves from 400.39 to 400.57 eV, while that of C–N group moves from 398.68 to 398.90 eV after adsorption (Fig. 10f). The above increasement of binding energy demonstrated the involvement of N and O for Cr(VI) adsorption by $Fe_3O_4@SiO_2$–G3. Because there are five electrons in the outer layer of the N atom, three of which have been paired to form bonds, the remaining pair of lone pairs are easy to provide a lone pair of electrons to form a complex. N shares electrons with Cr in this process, resulting in a decrease in electron density of N and an increase in binding energy. With the aid of electron donors, a large amount of Cr(VI) was reduced from Cr(VI) to Cr(III), which was then adsorbed. Meanwhile, O may also share electrons with Cr to form a coordination complex [43]. According to the above considerations, the number of N- and O-containing functional groups is the critical factor that determine the adsorption property of $Fe_3O_4@SiO_2$–G3.

3.8 Reusability

Reusability is an important parameter property for evaluating the performance of the adsorbent. The adsorption/desorption process of Cr(VI) on $Fe_3O_4@SiO_2$–G3 was investigated using 0.5 mol/L NaOH solution as eluent. The reusability property was determined by considering five adsorption–desorption cycles. Figure 11 shows that the Cr(VI) adsorption capacity of $Fe_3O_4@SiO_2$–G3 gradually decreases with the number of cycles, but not significantly. After five cycles of use, the removal ration of $Fe_3O_4@$

Fig. 10 The XPS total survey spectra of $Fe_3O_4@SiO_2$–G3 (**a**), high resolution Cr 2p spectrum (**b**), high resolution O 1s spectrum (**c**, **d**) and high resolution N 1s spectrum (**e**, **f**) before and after adsorption of Cr(VI)
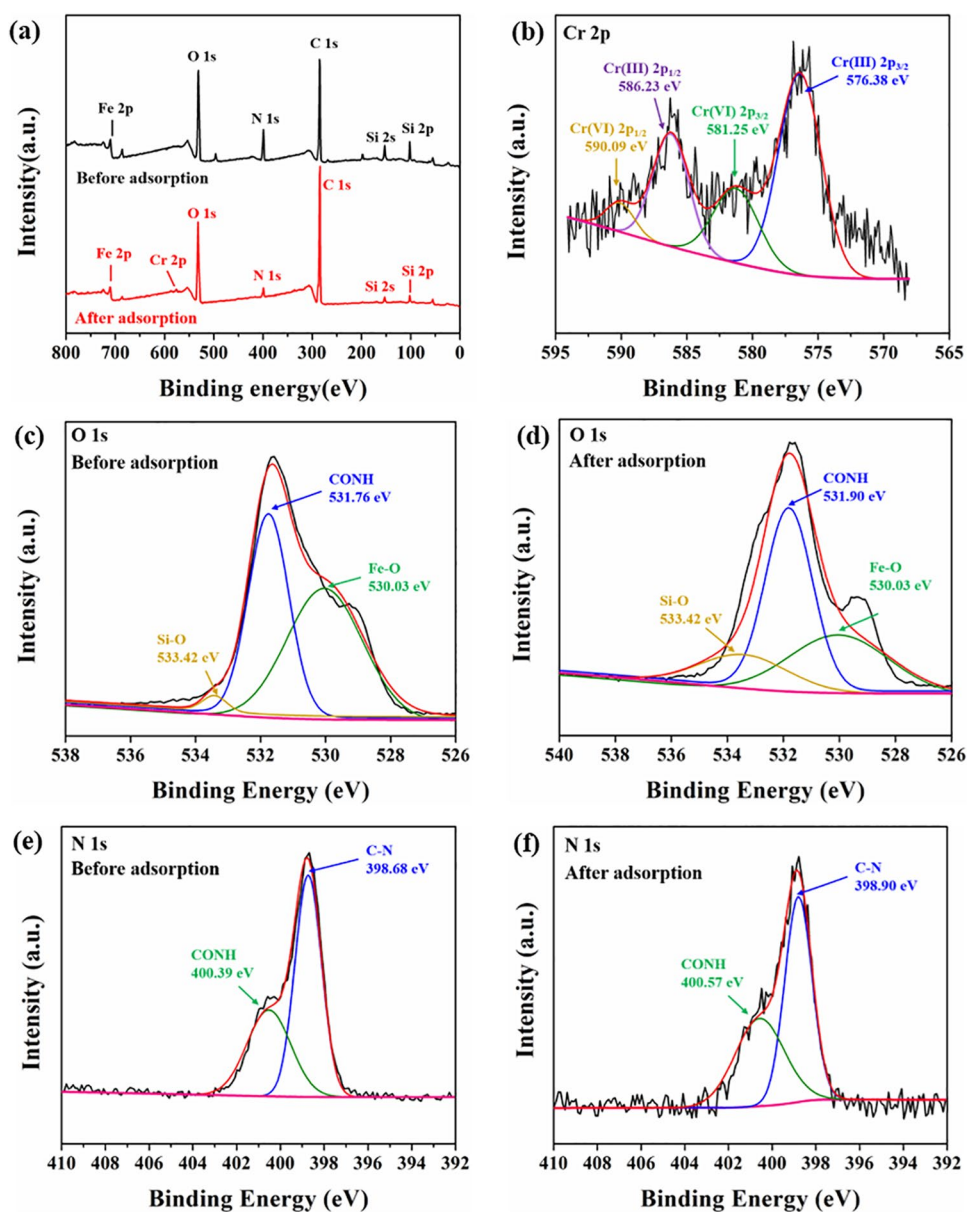
SiO_2–G3 for Cr(VI) remains above 89.5%, indicating that $Fe_3O_4@SiO_2$–G3 has good stability and reusability.

4 Conclusions

In this work, three different generations of PAMAM dendrimer immobilized on magnetic Fe_3O_4 composites ($Fe_3O_4@SiO_2$–G1, $Fe_3O_4@SiO_2$–G3, $Fe_3O_4@SiO_2$–G5) were successfully prepared and used to remove Cr(VI). The solution pH of 3.0 is favored for Cr(VI) removal. Adsorption approaches equilibrium at 60 min for all the adsorbents. The results of adsorption kinetics and isothermal studies indicate that the adsorption behavior conform to both the pseudo-second-order kinetic model (chemical interaction) and Langmuir isotherm model (homogeneous monolayer adsorption). Furthermore, the thermodynamics model demonstrates that adsorption is endothermic and spontaneous. More interestingly, we found that the uptake of Cr(VI) obeyed the sequence of $Fe_3O_4@SiO_2$–G1 $<$ $Fe_3O_4@SiO_2$–G5 $<$ $Fe_3O_4@SiO_2$–G3, indicating that the affinity of the nanocomposites increases with dendrimer generation increases only in low generation range, but excessively high generation of PAMAM is unfavourable for the adsorption due to the large steric hindrance and serious surface defects of PAMAM. As-synthesized $Fe_3O_4@SiO_2$–G3 exhibits competitive adsorption capacity (334.45 mg/g) for Cr(VI) than most alternative adsorbents mainly because of its regular structure and the abundant active sites located within its interior and its surface. Regeneration suggests the removal
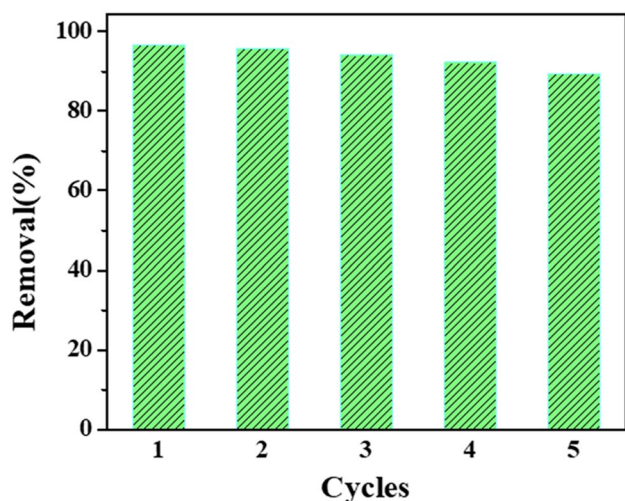
ration of Fe$_3$O$_4$@SiO$_2$–G3 for Cr(VI) remains above 89.5% after five cycles of adsorption–desorption. This work shows that Fe$_3$O$_4$@SiO$_2$–G3 is an efficient and reusable adsorbent for the adsorption of Cr(VI) from aqueous solution, and the obtained results could be useful for the generation optimization during fabrication of dendrimer modified adsorbents.

Declarations

Conflict of interest There are no conflict to declare.

References

1. S. Chowdhury, M.A.J. Mazumder, O. Al-Attas, T. Husain, Heavy metals in drinking water: occurrences, implications, and future needs in developing countries. Sci. Total Environ. **569**, 476–488 (2016)
2. M.L. Sall, A.K.D. Diaw, D. Gningue-Sall, S.E. Aaron, J.J. Aaron, Toxic heavy metals: impact on the environment and human health, and treatment with conducting organic polymers, a review. Environ. Sci. Pollut. R **27**(24), 29927–29942 (2020)
3. C. Donga, S.B. Mishra, A.S. Abd-El-Aziz, A.K. Mishra, Advances in graphene-based magnetic and graphene-based/TiO(2)nanoparticles in the removal of heavy metals and organic pollutants from industrial wastewater. J. Inorg. Organomet. P **31**(2), 463–480 (2020)
4. M. Balali-Mood, K. Naseri, Z. Tahergorabi, M.R. Khazdair, M. Sadeghi, Toxic mechanisms of five heavy metals: mercury, lead, chromium, cadmium, and arsenic. Front. Pharmacol. **12**, 643972 (2021)
5. S.P. Wu, X.Z. Dai, T.T. Cheng, S.J. Li, Highly sensitive and selective ion-imprinted polymers based on one-step electrodeposition of chitosan–graphene nanocomposites for the determination of Cr(VI). Carbohyd. Polym. **195**, 199–206 (2018)
6. H. Peng, J. Guo, Removal of chromium from wastewater by membrane filtration, chemical precipitation, ion exchange, adsorption electrocoagulation, electrochemical reduction, electrodialysis, electrodeionization, photocatalysis and nanotechnology: a review. Environ. Chem. Lett. **18**(6), 2055–2068 (2020)
7. B.H. Xie, C. Shan, Z. Xu, X.C. Li, X.L. Zhang, J.J. Chen, B.C. Pan, One-step removal of Cr(VI) at alkaline pH by UV/sulfite process: reduction to Cr(III) and in situ Cr(III) precipitation. Chem. Eng. J. **308**, 791–797 (2017)
8. Y.F. Ren, Y.H. Han, Q.Y. Zhang, A magnetic ion exchange resin with high efficiency of removing Cr (VI). Colloid Surf. A **604**, 125279 (2020)
9. G. Sharma, D. Pathania, M. Naushad, N.C. Kothiyal, Fabrication, characterization and antimicrobial activity of polyaniline Th(IV) tungstomolybdophosphate nanocomposite material: efficient removal of toxic metal ions from water. Chem. Eng. J. **251**, 413–421 (2014)
10. W. Jin, H. Du, S.L. Zheng, Y. Zhang, Electrochemical processes for the environmental remediation of toxic Cr(VI): a review. Electrochim. Acta **191**, 1044–1055 (2016)
11. G. Sharma, A. Kumar, M. Naushad, B. Thakur, D.V.N. Vo, B. Gao, A.A. Al-Kahtani, F.J. Stadler, Adsorptional-photocatalytic removal of fast sulphon black dye by using chitin-cl-poly(itaconic acid-co-acrylamide)/zirconium tungstate nanocomposite hydrogel. J. Hazard. Mater. **416**, 125714 (2021)
12. E. Doustkhah, S. Rostamnia, H.G. Hossieni, R. Luque, Covalently bonded PIDA on SBA-15 as robust Pd support: water-tolerant designed catalysts for aqueous suzuki couplings. ChemistrySelect **2**(1), 329–334 (2017)
13. Y.C. Zhu, C.C. Jiao, L.Q. Han, Y.H. Gao, S.J. Li, X.H. Yuan, A novel PHEMA-based bismuth oxide composite with high photocatalytic activity. J. Inorg. Organomet. P **30**(11), 4739–4752 (2020)
14. S. Gao, Z.C. Liu, Q.S. Yan, P. Wei, Y. Li, J.Y. Ji, L. Li, Facile synthesis of polypyrrole/reduced graphene oxide composite hydrogel for Cr(VI) removal. J. Inorg. Organomet. P. **31**(9), 3677–3685 (2021)
15. A. Mudhoo, D. Mohan, C.U. Pittman, G. Sharma, M. Sillanpaa, Adsorbents for real-scale water remediation: gaps and the road forward. J. Environ. Chem. Eng. **9**(4), 105380 (2021)
16. D. Mohan, C.U. Pittman, Activated carbons and low cost adsorbents for remediation of tri- and hexavalent chromium from water. J. Hazard. Mater. **137**(2), 762–811 (2006)
17. W.Z. Gu, D.C. Zheng, D.P. Li, C.C. Wei, X. Wang, Q.Z.M. Yang, C. Tian, M.Y. Cui, Integrative effect of citrate on Cr(VI) and total Cr removal using a sulfate-reducing bacteria consortium. Chemosphere **279**, 130437 (2021)
18. Y. Song, Z.X. Li, S.J. Shao, W.Z. Jiao, Y.Z. Liu, High-gravity intensified preparation of D201 resin-hydrated iron oxide nanocomposites for Cr(VI) removal. Adv. Powder Technol. **32**(5), 1584–1593 (2021)
19. B. Zhang, Y.H. Wu, Y. Fan, Synthesis of novel magnetic NiFe$_2$O$_4$ nanocomposite grafted chitosan and the adsorption mechanism of Cr(VI). J. Inorg. Organomet. P. **29**(1), 290–301 (2019)
20. H. Alamgholiloo, S. Rostamnia, K.Q. Zhang, T.H. Lee, Y.S. Lee, R.S. Varma, H.W. Jang, M. Shokouhimehr, Boosting aerobic oxidation of alcohols via synergistic effect between TEMPO and a composite Fe$_3$O$_4$/Cu–BDC/GO nanocatalyst. ACS Omega **5**(10), 5182–5191 (2020)

21. X.H. Yang, J.R. Kan, F.Y. Zhang, M.Y. Zhu, S.J. Li, Facile fabrication of Mn^{2+} doped magnetite microspheres as efficient electrode material for supercapacitors. J. Inorg. Organomet. P. **27**(2), 542–551 (2017)

22. E. Doustkhah, S. Rostamnia, B. Gholipour, B. Zeynizadeh, A. Baghban, R. Luque, Design of chitosan–dithiocarbamate magnetically separable catalytic nanocomposites for greener aqueous oxidations at room temperature. Mol. Catal. **434**, 7–15 (2017)

23. N.A. Jumat, S.H. Khor, W.J. Basirun, J.C. Juan, S.W. Phang, Highly visible light active ternary polyaniline-TiO_2–Fe_3O_4 nanotube/nanorod for photodegradation of reactive black 5 dyes. J. Inorg. Organomet. P. **31**(5), 2168–2181 (2021)

24. S. Rostamnia, B. Zeynizadeh, E. Doustkhah, A. Baghban, K.O. Aghbash, The use of K-carrageenan/Fe_3O_4 nanocomposite as a nanomagnetic catalyst for clean synthesis of rhodanines. Catal. Commun. **68**, 77–83 (2015)

25. Q. Chen, W.J. Wei, J.J. Tang, J.K. Lin, S.J. Li, M.Y. Zhu, Dopamine-assisted preparation of Fe_3O_4@MnO_2 yolk@shell microspheres for improved pseudocapacitive performance. Electrochim. Acta. **317**, 628–637 (2019)

26. J.F. Liu, Z.S. Zhao, G.B. Jiang, Coating Fe_3O_4 magnetic nanoparticles with humic acid for high efficient removal of heavy metals in water. Environ. Sci. Technol. **42**(18), 6949–6954 (2008)

27. G. Sharma, A. Kumar, S. Sharma, M. Naushad, P. Dhiman, D.V.N. Vo, F.J. Stadler, Fe_3O_4/ZnO/Si_3N_4 nanocomposite based photocatalyst for the degradation of dyes from aqueous solution. Mater. Lett. **278**, 128359 (2020)

28. S. Bagheri, A. Esrafili, M. Kermani, J. Mehralipour, M. Gholami, Performance evaluation of a novel rGO-Fe-0/Fe_3O_4-PEI nanocomposite for lead and cadmium removal from aqueous solutions. J. Mol. Liq. **320**, 114422 (2020)

29. E. Doustkhah, M. Heidarizadeh, S. Rostamnia, A. Hassankhani, B. Kazemi, X. Liu, Copper immobilization on carboxylic acid-rich Fe_3O_4–Pectin: Cu^{2+}@Fe_3O_4–Pectin a superparamagnetic nanobiopolymer source for click reaction. Mater. Lett. **216**, 139–143 (2018)

30. A. Zarei, S. Saedi, F. Seidi, Synthesis and application of Fe_3O_4@SiO_2@carboxyl-terminated PAMAM dendrimer nanocomposite for heavy metal removal. J. Inorg. Organomet. P. **28**(6), 2835–2843 (2018)

31. M. Nourmohammadi, S. Rouhani, S. Azizi, M. Maaza, T.A.M. Msagati, S. Rostamnia, M. Hatami, S. Khaksar, E. Zarenezhad, H.W. Jang, Magnetic nanocomposite of crosslinked chitosan with 4,6-diacetylresorci-nol for gold immobilization (Fe_3O_4@CS/DAR–Au) as a catalyst for an efficient one-pot synthesis of propargylamine. Mater. Today Commun. **29**, 102798 (2021)

32. F. Ke, J. Jiang, Y.Z. Li, J. Liang, X.C. Wan, S. Ko, Highly selective removal of Hg^{2+} and Pb^{2+} by thiol-functionalized Fe_3O_4@metal–organic framework core–shell magnetic microspheres. Appl. Surf. Sci. **413**, 266–274 (2017)

33. N. Alhokbany, T. Ahamad, M. Naushad, S.M. Alshehri, Feasibility of toxic metal removal from aqueous medium using Schiff-base based highly porous nanocomposite: adsorption characteristics and post characterization. J. Mol. Liq. **294**, 111598 (2019)

34. W. Fu, X.Y. Wang, Z.Q. Huang, Remarkable reusability of magnetic Fe_3O_4-encapsulated $C_3N_3S_3$ polymer/reduced graphene oxide composite: a highly effective adsorbent for Pb and Hg ions. Sci. Total Environ. **659**, 895–904 (2019)

35. B. Surekha, N.S. Kommana, S.K. Dubey, A.V.P. Kumar, R. Shukla, P. Kesharwani, PAMAM dendrimer as a talented multifunctional biomimetic nanocarrier for cancer diagnosis and therapy. Colloid Surf. B **204**, 111837 (2021)

36. M. Nikzamir, Y. Hanifehpour, A. Akbarzadeh, Y. Panahi, Applications of dendrimers in nanomedicine and drug delivery: a review. J. Inorg. Organomet. P. **31**(6), 2246–2261 (2021)

37. E.B. Bahadir, M.K. Sezginturk, Poly(amidoamine) (PAMAM): an emerging material for electrochemical bio(sensing) applications. Talanta **148**, 427–438 (2016)

38. H. Viltres, Y.C. Lopez, C. Leyva, N.K. Gupta, A.G. Naranjo, P. Acevedo-Pena, A. Sanchez-Diaz, J. Bae, K.S. Kim, Polyamidoamine dendrimer-based materials for environmental applications: a review. J. Mol. Liq. **334**, 116017 (2021)

39. B. Ren, K. Wang, B.S. Zhang, H.Y. Li, Y.Z. Niu, H. Chen, Z.L. Yang, X.Z. Li, H.Q. Zhang, HQ, Adsorption behavior of PAMAM dendrimers functionalized silica for Cd(II) from aqueous solution: experimental and theoretical calculation. J. Taiwan Inst. Chem. E **101**, 80–91 (2019)

40. M. Heidarizadeh, E. Doustkhah, F. Saberi, S. Rostamnia, A. Hassankhani, P.F. Rezaei, Silica nanostructures, a heterogeneous surface for dendrimer functionalization. ChemistrySelect **3**(25), 7137–7151 (2018)

41. Y. Mansourpanah, A. Ghanbari, H. Yazdani, A.G. Mohammadi, A. Rahimpour, Silver-polyamidoamine/graphene oxide thin film nanofiltration membrane with improved antifouling and antibacterial properties for water purification and desalination. Desalination **511**, 115109 (2021)

42. D.K. Cheng, X.H. Dai, L. Chen, Y.H. Cui, C.W. Qiang, Q. Sun, J.D. Dai, Thiol-yne click synthesis of polyamide-amine dendritic magnetic halloysite nanotubes for the efficient removal of Pb(II). ACS Sustain. Chem. Eng. **8**(2), 771–781 (2020)

43. L.P. Luan, B.T. Tang, Y.F. Liu, A.L. Wang, B.B. Zhang, W.L. Xu, Y.Z. Niu, Selective capture of Hg(II) and Ag(I) from water by sulfur-functionalized polyamidoamine dendrimer/magnetic Fe_3O_4 hybrid materials. Sep. Purif. Technol. **257**, 117902 (2021)

44. M. Mikhaylova, D.K. Kim, C.C. Berry, A. Zagorodni, M. Toprak, A.S.G. Curtis, M. Muhammed, BSA immobilization on amine-functionalized superparamagnetic iron oxide nanoparticles. Chem. Mater. **16**(12), 2344–2354 (2004)

45. S. Rostamnia, B. Gholipour, X. Liu, Y. Wang, H. Arandiyan, NH_2-coordinately immobilized tris(8-quinolinolato)iron onto the silica coated magnetite nanoparticle: Fe_3O_4@SiO_2–FeQ(3) as a selective Fenton-like catalyst for clean oxidation of sulfides. J. Colloid. Interf. Sci. **511**, 447–455 (2018)

46. P. Dhiman, S. Sharma, A. Kumar, M. Shekh, G. Sharma, M. Naushad, Rapid visible and solar photocatalytic Cr(VI) reduction and electrochemical sensing of dopamine using solution combustion synthesized ZnO–Fe_2O_3 nano heterojunctions: mechanism elucidation. Ceram. Int. **46**(8), 12255–12268 (2020)

47. W.M. Liu, Y.N. Xue, N. Peng, W.T. He, R.X. Zhuo, S.W. Huang, Dendrimer modified magnetic iron oxide nanoparticle/DNA/PEI ternary magnetoplexes: a novel strategy for magnetofection. J. Mater. Chem. **21**(35), 13306–13315 (2011)

48. J. Shang, Y.N. Guo, D.L. He, W. Qu, Y.N. Tang, L. Zhou, R.L. Zhu, A novel graphene oxide-dicationic ionic liquid composite for Cr(VI) adsorption from aqueous solutions. J. Hazard. Mater. **416**, 125706 (2021)

49. G. Sharma, B. Thakur, A. Kumar, S. Sharma, M. Naushad, F.J. Stadler, Atrazine removal using chitin-cl-poly(acrylamide-co-itaconic acid) nanohydrogel: isotherms and pH responsive nature. Carbohyd. Polym. **241**, 116258 (2020)

50. N. Rezak, A. Bahmani, N. Bettahar, Adsorptive removal of P(V) and Cr(VI) by calcined Zn–Al–Fe ternary LDHs. Water Sci. Technol. **83**(10), 2504–2517 (2021)

51. T.F. Guo, H.N. Gu, S.C. Ma, N. Wang, Increasing phosphate sorption on barium slag by adding phosphogypsum for non-hazardous treatment. J. Environ. Manag. **270**, 110823 (2020)

52. J.J. Yang, Z.F. Zhang, W.T. Pang, H.J. Chen, G.Q. Yan, Polyamidoamine dendrimers functionalized magnetic carbon nanotubes as an efficient adsorbent for the separation of flavonoids from plant extraction. Sep. Purif. Technol. **227**, 115710 (2019)

53. G. Sharma, T.S. AlGarni, P.S. Kumar, S. Bhogal, A. Kumar, S. Sharma, M. Naushad, Z.A. ALOthman, F.J. Stadler, Utilization of Ag_2O–Al_2O_3–ZrO_2 decorated onto rGO as adsorbent for the removal of Congo red from aqueous solution. Environ. Res. **197**, 111179 (2021)

54. W.J. Shen, Y. Mu, T. Xiao, Z.H. Ai, Magnetic Fe_3O_4–FeB nanocomposites with promoted Cr(VI) removal performance. Chem. Eng. J. **285**, 57–68 (2016)

55. Y. Zhang, Y.Y. Mo, T. Vincent, C. Faur, E. Guibal, Boosted Cr(VI) sorption coupled reduction from aqueous solution using quaternized algal/alginate@PEI beads. Chemosphere **281**, 130844 (2021)

56. H.S. Ramadan, M. Mobarak, E.C. Lima, A. Bonilla-Petriciolet, Z.C. Li, M.K. Seliem, Cr(VI) adsorption onto a new composite prepared from Meidum black clay and pomegranate peel extract: experiments and physicochemical interpretations. J. Environ. Chem. Eng. **9**(4), 105352 (2021)

57. M.B. Poudel, G.P. Awasthi, H.J. Kim, Novel insight into the adsorption of Cr(VI) and Pb(II) ions by MOF derived Co–Al layered double hydroxide @hematite nanorods on 3D porous carbon nanofiber network. Chem. Eng. J. **417**, 129312 (2021)

58. L.L. Du, P. Gao, Y.L. Liu, T. Minami, C.B. Yu, Removal of Cr(VI) from aqueous solution by polypyrrole/hollow mesoporous silica particles. Nanomaterials **10**(4), 686 (2020)

59. Y. Yang, Y.H. Zhang, G.Y. Wang, Z.B. Yang, J.R. Xian, Y.X. Yang, T. Li, Y.L. Pu, Y.X. Jia, Y. Li, Z. Cheng, S.R. Zhang, X.X. Xu, Adsorption and reduction of Cr(VI) by a novel nanoscale FeS/chitosan/biochar composite from aqueous solution. J. Environ. Chem. Eng. **9**, 105407 (2021)